

## RESEARCH ARTICLE OPEN ACCESS

# Atomic-Scale Epitaxy for Tailoring Crystalline GeSbTe Alloys Into Bidimensional Phases

Valeria Bragaglia<sup>1</sup>  | Fabrizio Arciprete<sup>1,2,3</sup> | Simone Prili<sup>2,3</sup>  | Yukihiko Takagaki<sup>1</sup> | Antonio Massimiliano Mio<sup>4</sup> | Riccardo Mazzarello<sup>5</sup> | Jos Emiel Boschker<sup>1,6</sup> | Raffaella Calarco<sup>1,3</sup> 

<sup>1</sup>Paul-Drude-Institut Für Festkörperelektronik Hausvogteiplatz 5–7, Berlin, Germany | <sup>2</sup>Dipartimento Di Fisica, Università degli Studi di Roma “Tor Vergata”, Rome, Italy | <sup>3</sup>Istituto Per La Microelettronica e Microsistemi (IMM), Consiglio Nazionale delle Ricerche, Rome, Italy | <sup>4</sup>Istituto Per La Microelettronica e Microsistemi (IMM), Consiglio Nazionale delle Ricerche, Zona Industriale, Catania, Italy | <sup>5</sup>Dipartimento Di Fisica, Università degli Studi di Roma “La Sapienza”, Rome, Italy | <sup>6</sup>Ferdinand-Braun-Institut (FBH), Berlin, Germany

**Correspondence:** Valeria Bragaglia ([vbr@zurich.ibm.com](mailto:vbr@zurich.ibm.com)) | Simone Prili ([prili@roma2.infn.it](mailto:prili@roma2.infn.it)) | Raffaella Calarco ([Raffaella.Calarco@artov.imm.cnr.it](mailto:Raffaella.Calarco@artov.imm.cnr.it))

**Received:** 10 October 2025 | **Revised:** 18 November 2025 | **Accepted:** 19 November 2025

**Keywords:** epitaxy | molecular beam epitaxy | phase change materials | topological insulators | vacancy ordering

## ABSTRACT

In this study, we establish an accurate growth diagram—describing the phase, composition, and atomic stacking of Ge-Sb-Te alloys (GST)—that can be used as a prediction tool for thin film deposition. This framework for epitaxy at the atomic scale allows for designing tailored crystalline GST phases with precise atomic layer stacking configurations. By leveraging insights into phase stability, we optimize growth conditions to achieve high-quality, bidimensional GST structures of different compositions ( $\text{Ge}_2\text{Sb}_2\text{Te}_5$ ,  $\text{Ge}_3\text{Sb}_2\text{Te}_6$ , and  $\text{Ge}_1\text{Sb}_2\text{Te}_4$ ) and phases (ordered-cubic and trigonal). Moreover, we examine the influence of structural anisotropies and interface effects on the low-temperature magneto-transport properties. The orientational ordering of the vacancy layers and their evolution into van der Waals gaps alters the electrical conduction dramatically, plausibly also in the presence of the topological surface states and their coupling with the bulk states. In addition, we examine the reversible transition between two stable resistance states in a memory cell for the GST precisely tailored by the growth using Molecular Beam Epitaxy (MBE). Its textured structure favors low power consumption, making it a promising candidate for phase-change memory technology.

## 1 | Introduction

Research on the topological electronic states realized in topological insulators (TIs) is a crucial topic bearing relevant impact for fundamental physics as well as for potential applications [1–4]. 3D TI compounds  $\text{Sb}_2\text{Te}_3$  [5–7],  $\text{Bi}_2\text{Te}_3$  [7] and  $\text{Bi}_2\text{Se}_3$  [7] have been widely studied both theoretically and experimentally in the past decade. Moreover, the presence of topological states was also predicted for GeSbTe alloys (GST) and GST-based superlattices [8]. These materials are especially interesting, and the influences of the topological states on their electrical properties are particularly crucial due to their mature usage for storage appli-

cations [8, 9] and their more recent prospects for neuromorphic computing [10, 11].

GST alloys present one amorphous (a-) and two crystalline (x-) phases: a metastable, cubic rocksalt-like (c-GST), and a stable trigonal one (t-GST). Typically, the alloy contains, depending on composition, about 25% of intrinsic Ge/Sb-vacancies. The two x-phases consist of a sequence of Te and Ge/Sb planes alternately stacked along the [111] crystallographic direction. The main difference between these two crystalline structures lies in their configuration of vacancies: In c-GST, they are randomly distributed in the Ge/Sb cation layers, whereas in t-GST, they

This is an open access article under the terms of the [Creative Commons Attribution](https://creativecommons.org/licenses/by/4.0/) License, which permits use, distribution and reproduction in any medium, provided the original work is properly cited.

© 2025 The Author(s). *Advanced Materials Interfaces* published by Wiley-VCH GmbH

are periodically arranged into pseudo-van der Waals gaps (vdW) in between two adjacent Te layers [12, 13]. In between the two x-phases, an intermediate “ordered-cubic” phase can be found, in which the vacancies gradually increase their ordering into planes [14–16]. Then, by a global in-plane shift of adjacent GST building blocks relative to each other, the vacancy layers (VLs) convert into vdW-like gaps. Recent in situ TEM observations [17] directly visualized this process, showing that the transition from the ordered cubic to the trigonal phase proceeds via a shear-type collapse of the VLs into vdW-like gaps through block shifts of atomic planes. A large change of the resistance occurs in association with the ordering process, which is responsible for the metal-insulator transition (MIT) between the amorphous and crystalline phase and for the additional decrease of resistance once the “ordered-cubic” phase transforms into the trigonal one [18, 19].

It is unclear whether the gradual ordering and/or the in-plane shifts lead to a transition between topologically distinct phases. First-principles calculations indicate that crystalline x-GST alloys exhibit different TI properties depending on their layer stacking sequence and composition [9, 20, 21]. The first prediction of a TI phase in  $\text{Ge}_2\text{Sb}_2\text{Te}_5$  (GST225) was made by Kim et al. for the Petrov [22] stacking, whereas the most energetically favorable structure, the Kooi and De Hosson (KH) [23] structure, was predicted to be topologically trivial [20]. Nevertheless, by density functional theory (DFT), it has been calculated that under small pressure [24] or strain [25], even the KH phase of GST225 can be a TI. Additionally, Silkin et al., have calculated the band structure for the stable t-GST225, showing that TI properties do not depend on the specific location of the Ge and Sb atoms in the cation sublattice, but do depend on their relative concentration within the layer [26]. The precise stoichiometry is thus relevant. Furthermore, in a theoretical study by Kim et al. [27], the electronic properties in c-GST225 were investigated upon introducing different types of disorder in the cationic sublattice (Ge, Sb migration into vacancy layers and Ge-Sb exchange). It has been shown that the TI properties vary with the formation of ordered cationic layers, which may be linked to the MIT observed in GST as a function of the annealing temperature [14, 18, 28, 29]. However, excess Ge/Sb vacancies responsible for self-doping effects were not included in these models. Furthermore, the MIT was theoretically and experimentally shown to be of Anderson type and to be driven by the ordering of the vacancies [14, 18, 28].

To study and experimentally validate the theoretical predictions, the use of ideally perfect, single-crystalline GST is critical for observing the TI properties. Conscious of this need, we have developed the epitaxial growth of GST-based alloys using MBE [30]. This achievement allowed for the first experimental studies of the band structure of GeTe [31, 32] and GST [33] by angle-resolved photoemission spectroscopy. Recent years have witnessed the increased activity in the epitaxial growth of phase change materials [34–37], which results in the superior crystalline quality manifested as the single vertical epitaxial orientation, well-defined interfaces, and ordered distribution of vacancies along the (111) growth direction. In a recent publication, we have shown that such films have made it possible to directly correlate the vacancy ordering in the crystalline structure to the MIT in GST [18, 19]. This result has been obtained by comparing the electrical and structural properties of GST sam-

ples annealed at different temperatures, therefore exhibiting different degrees of vacancy ordering. Furthermore, the resistivity window is enlarged by at least one order of magnitude by employing epitaxially grown GST instead of polycrystalline GST [18]. This provides intriguing perspectives for the resistive switching applications, such as the realization of multilevel memory devices. Additionally, recent studies highlighted that vacancy ordering has a significant influence on GST optical properties [38], especially reflectivity, thus opening up the possibility of employing such engineered structures for optical applications.

The necessity of designing x-GST by tuning phase, composition, and vacancy ordering on demand is thus given. In this paper, we take a step toward this goal by presenting a first-ever phase diagram for the epitaxial x-GST prepared by MBE. We demonstrate that the variety in the GST compositions and phases can be distinguished from each other using the transport properties. We discuss how the surface, bulk, and interface states affect the transport at low temperatures. Furthermore, a fundamental change is found to occur in the quantum transport during the transition between the cubic and trigonal phases. To be specific, the transport in the t-phase is found to be highly unusual. Finally, we evaluate the potential of epitaxial GST for memory devices.

## 2 | Results and Discussion

The epitaxial growth of GST alloys is challenging due to the complex interplay between composition, phase, and ordering [18]. Controlling these three properties is essential to obtain a material with well-defined physical properties. In our previous study [16], we combined Raman spectroscopy and X-ray diffraction (XRD) to systematically investigate the impact of growth temperature and Ge:Sb:Te flux ratio on the phase and composition of epitaxial GST films. This cross-correlation analysis allowed us to establish the link between growth parameters, crystalline phase, and composition. Based on these results, in Figure 1a, we present a growth diagram used to select the right growth conditions to deposit GST alloys with tailored properties. In the diagram, the Te flux ( $\Phi_{\text{Te}}$ ) is plotted as a function of the substrate temperature ( $T_{\text{sub}}$ ). All sample growths are performed under comparable Ge and Sb fluxes ( $\Phi_{\text{Ge}} = 0.055$  nm/min,  $\Phi_{\text{Sb}} = 0.193$  nm/min). The details of the structural characterization leading to the identification of each phase reported in the diagram are thoroughly discussed in ref [16], although alternative valuable approaches can be found in the literature [39].

The samples are distinguished by x-phase (cubic, trigonal, and mixed) and composition. Squares are associated with samples in the c-phase, circles with the t-phase, and mixed samples are represented by both symbols. Dashed and dot-dashed lines (mere guides for the eye) delimit the different phase regions. Three main regions can be identified depending on the composition GST124, 225, and 326 (labeled in blue, orange, and violet, respectively). The whole delimited 225 region is colored in orange to help the reader. Samples with mixed composition (denoted by two colors on the respective symbol) are also obtained and are positioned on the boundaries of the colored regions in Figure 1a; these boundary regions are not sharp.

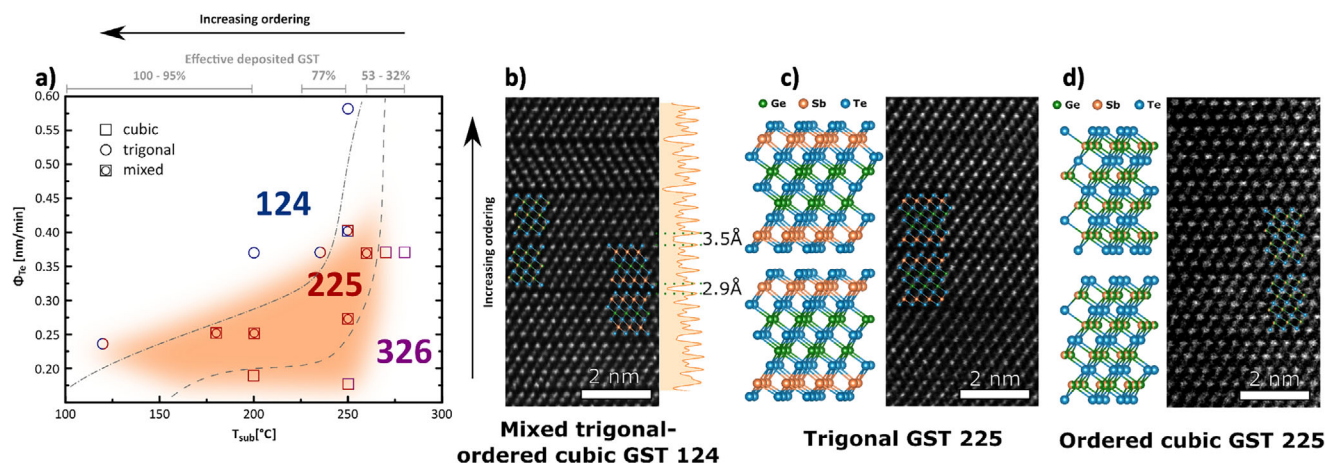


**FIGURE 1** | (a) Growth diagram for GST displaying crystalline phases and compositions upon  $\Phi_{\text{Te}}$  and  $T_{\text{sub}}$  variation. Square symbols stand for c- and circles for t-phase, while mixed phases are represented by both symbols. Dashed and dot-dashed lines are drawn as a guide for the eye to delimit the different phase regions. GST124, 225, and 326 are distinguished by labels in three colors, blue, orange, and violet, respectively. The whole delimited 225 region is colored in orange to help the reader. On the top part of the diagram, the effective deposited GST material is given in percentage with respect to the nominal thickness. (b), (c) and (d) HAADF STEM micrographs of GST samples in mixed trigonal/ordered cubic GST124, trigonal GST225, and ordered cubic GST225 phases, respectively. Samples are oriented along the  $[1-10]$  zone axis (Z.A.) for the cubic/rocksalt phase and along the  $[\bar{1}1-20]$  Z.A. for the trigonal phase (hexagonal notation). For each sample, the corresponding crystal structure schematic is presented and overlapped with its micrograph (green, orange, and blue circles for Ge, Sb, and Te, respectively). In (b), a line intensity profile along the vertical axis is also shown, highlighting a vacancy gap of 2.9 and 3.5 Å for trigonal and ordered cubic phases, respectively. In (d), the crystalline GST is obtained by annealing a-GST.

In Figure 1a, the ordering of vacancies improves for increasing  $\Phi_{\text{Te}}$ , as evidenced by the transition from c- to t-GST, within a large range of  $T_{\text{sub}}$  between 180 and 250°C. Similarly, at constant  $\Phi_{\text{Te}}$ , the phase evolves from c-GST to t-GST for decreasing  $T_{\text{sub}}$ . At lower  $T_{\text{sub}}$ , more Te sticks on the sample surface and it is thus incorporated more efficiently. The same argument holds for increasing  $\Phi_{\text{Te}}$  at fixed  $T_{\text{sub}}$ . At lower  $\Phi_{\text{Te}}$ , ordering of the samples is more difficult, e.g., if  $\Phi_{\text{Te}} < 0.20$  nm/min, only c- or mixed phases are obtained, and at  $\Phi_{\text{Te}} \sim 0.25$  nm/min, there is a very large growth window in which only mixed phases can be grown. For  $\Phi_{\text{Te}} \sim 0.25$  nm/min, the stable t-phase is obtained only if  $T_{\text{sub}}$  is lower than about 175°C. Such results point out that the amount of  $\Phi_{\text{Te}}$  regulates the kinetics of ordering during the growth [16]. The deficit of Te prevents the ordering in the epitaxial film, making the c-phase more likely to appear. The 225 composition is recognized to be the most favorable one for GST, followed by the 124 and 326 compositions. GST225 is mostly obtained in the c- or mixed x-phase, whereas GST124 forms the t-phase.

Interestingly, the annealing of a-GST225 [19] samples leads to mixed x-phases with different compositions. This is in agreement with literature results obtained for the polycrystalline GST [23], where the segregation of GST124 from GST225 was proposed to occur to lower the total energy by the transition to the t-phase. Therefore, GST124 is indicated to be the most stable composition in the t-phase regardless of the preparation method. This can be intuitively understood considering that GST alloys lie on the pseudobinary line connecting GeTe and  $\text{Sb}_2\text{Te}_3$ ; these binary compounds present no vdW gaps (GeTe) or the most ordered alternation of vdW gaps ( $\text{Sb}_2\text{Te}_3$ ), and GST124 is the most  $\text{Sb}_2\text{Te}_3$ -rich composition among the three shown in Figure 1.

In summary, we observe that, for epitaxial growth, the preferred interfacial stacking of GST is related to the imposed stoichiometry,

independently of temperature. The three stoichiometries GST124, GST225, and GST326 correspond to a transition from trigonal to ordered-cubic ground state.

Local structural analysis on these x-GST samples was performed by Scanning Transmission Electron Microscopy (STEM) in High-Angle Annular Dark Field (HAADF) mode. Figure 1b,c correspond to the mixed trigonal/ordered cubic GST124 and the trigonal GST225, respectively. The samples are oriented along the  $[1-10]$  zone axis (Z.A.) in the case of the cubic/rocksalt phase and along the  $[\bar{1}1-20]$  Z.A. for the case of the trigonal phase (hexagonal notation).

As shown by the corresponding crystal structure schematic, depending on sample preparation, both trigonal and ordered cubic phases can be present, even in adjacent regions of the same sample. The line intensity profiles in Figure 1b show that the distance between the Te-Te planes at the van der Waals gap/VL is 2.9 and 3.5 Å for the trigonal and ordered cubic phases, respectively. This confirms that the different GST phases are characterized not only by the different structural ordering of the Ge/Sb-Te layers, but also by the change in the gap size. An ordered cubic phase has also been obtained during annealing of a-GST, as shown in Figure 1d.

We have investigated the influence of the composition and the crystalline structure of GST on the quantum transport properties. The presence of the topological surface states and their role in the electrical conduction can be examined in the low-temperature transport properties by analyzing the quantum effects. Figure 2 shows the change of the sheet conductivity  $\sigma_{\text{xx}}$  of GST films induced by a magnetic field at a temperature of 4.2 K. Here, the two samples in the c-phase with ordered vacancies are of the 225 and 326 compositions, and the other two samples in the t-phase

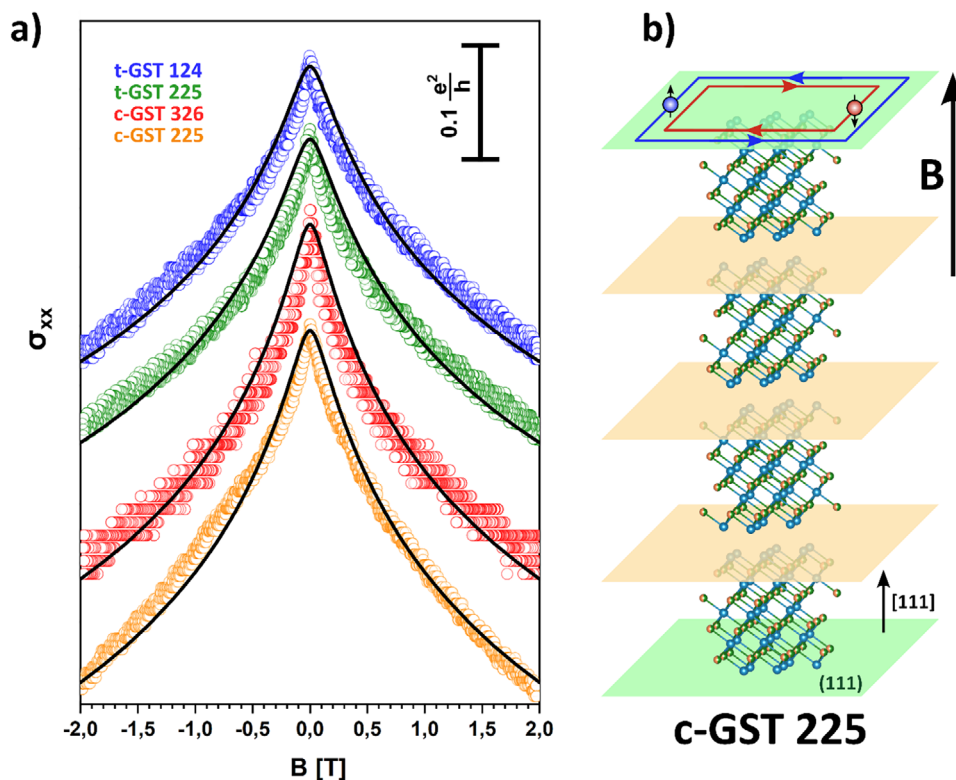


**FIGURE 2** | (a) Sheet conductivity  $\sigma_{xx}$  with perpendicular magnetic field  $B$ . The curves were obtained for c-GST225, c-GST326, t-GST225, and t-GST124 at a temperature of 4.2 K. The experimental data are plotted with circles, and the black lines show the result of the fitting using Equation (1). The result of the fits for all four samples is reported in Table 1. (b) Atomic arrangement of ordered c-GST225 in a layered configuration. The yellow planes located at the VLs highlight the conductive anisotropic channels at the interfaces. The green planes at the top and bottom of the structure represent TI surfaces with surface conduction channels, with red and blue arrows showing the movement of charge carriers.

**TABLE 1** | Sheet hole concentration ( $p_{\text{sheet}}$ ), sheet conductivity ( $\sigma_{xx}$ ), 3D hole concentration ( $p_{3D}$ ), thickness ( $t$ ), resistivity ( $\rho$ ), mobility ( $\mu$ ),  $\alpha$  parameter, phase coherence length ( $L_\phi$ ), phase coherence time ( $\tau_\phi$ ), Nyquist time ( $\tau_N$ ), and  $\tau_\phi/\tau_N$  ratio as obtained from magneto transport measurement at 4.2 K for four GST samples with different composition and order degree.

Samples	$P_{\text{sheet}}$ ( $\text{m}^{-2}$ )	$\sigma_{xx}$ (mS)	$P_{3D}$ ( $\text{m}^{-3}$ )	$t$ (nm)	$\rho$ ( $\Omega \text{ m}$ )	$\mu$ ( $\text{m}^2/\text{Vs}$ )	$\alpha$	$L_\phi$ (nm)	$\tau_\phi$ (ps)	$\tau_N$ (ps)	$\tau_\phi/\tau_N$
t-GST124	$5.3 \cdot 10^{19}$	19.6	$5.3 \cdot 10^{26}$	100	$5.2 \cdot 10^{-6}$	$2.3 \cdot 10^{-3}$	-0.430	57	8.9	170	0.053
t-GST225	$4.2 \cdot 10^{19}$	18.5	$4.2 \cdot 10^{26}$	100	$5.4 \cdot 10^{-6}$	$2.7 \cdot 10^{-3}$	-0.450	56	8.5	160	0.054
c-GST326	$4.7 \cdot 10^{19}$	2.8	$1.0 \cdot 10^{27}$	46	$1.6 \cdot 10^{-5}$	$3.8 \cdot 10^{-4}$	-0.485	61	40	37	1.08
c-GST225	$2.9 \cdot 10^{19}$	1.2	$9.7 \cdot 10^{26}$	30	$2.5 \cdot 10^{-5}$	$2.6 \cdot 10^{-4}$	-0.500	59	56	21	2.74

are of the 225 and 124 compositions. The thickness  $t$  of the films is provided in Table 1. The electrical conduction in the substrates can be ignored as the GST films were grown on undoped Si. The magnetic field  $B$  was applied perpendicular to the films. The films exhibited the negative magnetoconductivity resulting from the quantum interference effect at low temperatures [40]. Due to the large atomic numbers for Sb and Te, the spin-orbit coupling is strong in GST. The quantum interference thus gives rise to the weak antilocalization (WAL) effect. We have fitted the change of the conductivity  $\Delta\sigma_{xx}$  in the experimental data, which are shown

by the circles, using a 2D WAL theory, as shown by the black curves. The fitting was carried out using the following equation from ref. [41]

$$\Delta\sigma_{xx}(B) = \alpha \frac{e^2}{\pi h} \left[ \ln \left( \frac{l_B^2}{4L_\phi^2} \right) - \Psi \left( \frac{1}{2} + \frac{l_B^2}{4L_\phi^2} \right) \right] \quad (1)$$

where  $\Psi(x)$  is the digamma function,  $L_\phi$  is the phase coherence length and  $l_B = \sqrt{\frac{\hbar}{eB}}$  is the magnetic length. The values of  $L_\phi$

obtained by the fitting are shown in Table 1. The use of the 2D theory is justified as  $L_{\phi}$  is longer than, or at least comparable to, the film thickness. The WAL correction to the conductivity is described by Equation (1) for the 2D conduction, both in the bulk states of the films and in the topological surface states. The parameter  $\alpha$  counts the number of independently conducting channels and thus provides information on whether the surface state of TI is present in addition to the bulk state. Only the bulk state contributes to the conduction for conventional conductors, giving rise to  $\alpha = \frac{1}{2}$ . For the topological states, on the other hand,  $\alpha = 1$  is expected as two surface states are present with one state at each side of the layer.

Here, complications arise when the Fermi level is displaced from the Dirac point of the TI surface states to the conduction or valence band of the bulk states by carrier doping. Although the topological protection for TIs prevents the direct scattering between the two surface states, the scattering is not forbidden between the surface and bulk states. Holes can be scattered between the surface states through the bulk state in the circumstance that the bulk state is additionally occupied [42]. Changes in the value of  $\alpha$ , therefore, reflect the degree of the surface-bulk mixing in the layer. In the limit of the strong mixing,  $\alpha = \frac{1}{2}$  is realized as the whole system acts as a single conduction channel, resembling the non-TI conductors.

Experimentally,  $\alpha \sim \frac{1}{2}$  was found for all four types of samples in Figure 2a, see Table 1. It is noted, first of all, that there is a study [43] in which the part of the TI layer interfaced to the substrate was reported to be strongly disordered to the extent of causing the destruction of the surface state for the bottom side of the layer. This possibility can be ruled out as the epitaxially grown GST layers show an outstanding degree of structural quality, both in terms of the crystallinity and the sharpness of the interface with the substrate. Furthermore, the bulk subbands for ultrathin films may produce a weak-localization-like effect, compensating partly for the WAL effect, with the consequence of reducing the value of  $\alpha$ . Such a subband effect, however, can be ignored for the thickness of our GST layers.

In Table 1 the sheet hole concentration  $p_{\text{sheet}}$ , holes 3D concentration  $p_{3D}$ , electrical resistivity  $\rho$ , and mobility  $\mu$  obtained by Hall measurements using the van-der-Pauw method are summarized. The measurements were carried out at a temperature of 4.2 K. The phonon scattering is negligible at low temperature, and so the mobility was set primarily by the disorder in the layers. The carrier concentrations of the four samples are comparable to be on the order of  $10^{26} \text{ m}^{-3}$ . Such relatively large values stem from well-known self-doping effects due to non-stoichiometric vacancies and other extrinsic defects. The mobility for the t-GST samples was one order of magnitude higher than that of the c-GST samples, suggesting better crystalline order for the t phase than that for the c phase.

Though for all samples we obtain a value of  $\alpha = \frac{1}{2}$ , indicating the possible presence of delocalized bulk states leading to a single TI state, at the same time we observe a clear difference in mobility between c- and t-samples, which could be attributed to the degree of order in the samples.

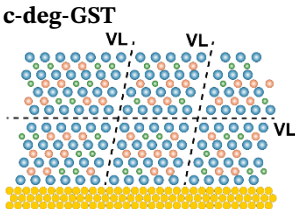
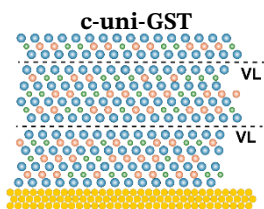
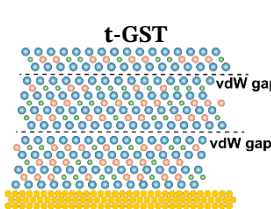
It has been shown [14] that the resistivity of epitaxially grown c-GST behaves exactly like in multi-grain t-samples in terms of resistivity, slope, and values, suggesting the presence of similar boundaries, which are in our case due to degenerate VLs [15, 18, 43].

Based on the experimental studies [18, 44] and the theoretical prediction [14], the observed abrupt drop of the resistivity between c- and t-samples is attributed to the reconfiguration of degenerate VLs into pseudo-vdW layers. The limited conduction in c-GST is likely more isotropic due to the presence of degenerate vacancy planes. In fact, within a dedicated transmission electron microscopy-based study, it has been demonstrated that, due to symmetry reasons, c-GST presents degenerate vacancy planes along all the equivalent  $\{111\}$  family of planes, as opposed to the t-phase, which only admits vacancy planes oriented in the  $[0001]$  direction [44]. Hence, the formation of vacancy planes in all equivalent  $\{111\}$  planes is predicted to make the conductivity increasingly isotropic (c-deg-GST). Conversely, upon further vacancy ordering, the conduction gradually becomes more anisotropic-like as the vacancies reorganize in VLs ordered only along the  $[111]$  direction, thus forming unidirectionally ordered cubic-GST (c-uni-GST). Eventually, upon transition of the c-uni-GST into the t-phase, the alloy evolves into the most metallic and anisotropic phase. For the isotropic conduction in c-deg-GST, the rate of the scattering events is likely to be high for the conduction holes due to the less regularity in the ordering of the vacancy planes. In addition, there is no propagation direction in which the holes do not have to encounter the vacancy planes.

Thus, the isotropic-like conduction in c-deg-GST may lead to a high rate of scattering events between bulk and surface states, unlike the anisotropic-dominated conduction in t-GST, where surface and bulk channels are more decoupled. The mobility for the t-phase is indeed one order of magnitude higher than that for the c-phase in Table 1, which also suggests that anisotropic processes contribute to the conduction in t-GST. These experimental findings would call for accurate simulations to determine the impact of the stacking order, Ge/Sb mixing, and excess vacancies on the transport properties; therefore, this must be clarified. At the same time, this behavior is consistent with earlier reports on GST transport properties, where a decrease in carrier mobility with increasing hole concentration was attributed to enhanced scattering processes [45, 46]. Together with Anderson localization effects promoted by structural disorder in cubic GST, such scattering mechanisms could explain the reduced mobility observed in our GST films. We summarize three possible scenarios for the ordering in the GST layer in Table 2.

The change in the electronic scattering between the c- and t-GSTs manifested as the mobility difference seems to be relevant also for the quantum transport properties in the WAL effect. Although the values of  $L_{\phi}$  are fairly similar among the four GST films, this is actually unexpected as  $\Delta\sigma_{xx}$  is substantially different between the c- and t-GST films. In order to compare the experimental values with theoretical predictions, we have calculated the phase coherence time as  $\tau_{\phi} = \frac{L_{\phi}^2}{D}$ , where  $D$  is the diffusion constant. In obtaining the values shown in Table 1, the effective mass of the holes was assumed to be the free electron mass in the calculation

TABLE 2 | Systematic depiction of transport-relevant structural properties.

Isotropic/Anisotropic Effects	Systems / Samples		
	c-deg-GST	c-uni-GST	t-GST
			
Atomic structure	VLs in equivalent {111} family planes	VLs only along the [111] direction	vdW layers only along the [111] direction

of  $D$ . The phase breaking in the 2D electron-electron scattering is expected to be given by the Nyquist dephasing rate from ref [47]

$$\tau_N^{-1} = k_B T \frac{e^2 \rho_s}{2\pi \hbar^2} \ln \left( \frac{\pi \hbar}{e^2 \rho_s} \right) \quad (2)$$

As one finds in the ratio  $\tau_\phi/\tau_N$  in Table 1, the dephasing in the c-GST films is governed by the Nyquist scattering process, as expected. In contrast, a significant discrepancy is found between the experiment and theory for the t-GST films. The origin of the disagreement is unclear at present. We point out that the possibility that the topological surface states have influenced the dephasing in an unusual manner for the t-GST films cannot be ruled out.

Additionally, to ascertain and validate the presence of the {111} family of planes in c-GST, we successfully induced the formation of an ordered c-phase through thermal annealing, with vacancy layers aligned along the  $\langle 111 \rangle$  directions.

Figure 3 reports the structural arrangement for the ordered cubic phase obtained by annealing at 170°C. Initially, the material was deposited on Sb-passivated Si(111) in the amorphous state. Upon annealing, the crystallization from the amorphous phase began at the interface to the substrate, leading to the formation of polycrystalline GST with VLs developing in the  $\langle 111 \rangle$  directions. The three stages in the progress of the crystallization from the as-deposited amorphous state to the fully crystallized polycrystalline GST phase are illustrated in Figure 3a. Figure 3b provides an atomic representation of the disordered rocksalt GST structure, depicting its cubic arrangement with a focus on the  $\langle 111 \rangle$  orientation containing 4 different equivalent {111} planes in which vacancies can be ordered. The elements Ge, Sb, and Te are color-coded in green, orange, and blue, respectively, showing their spatial arrangement within the lattice.

Experimentally, the maximum number of these planes that can be present in the same micrograph is two, clearly depending on the Z.A. In Figure 3c, indeed, two  $\langle 111 \rangle$  directions (i.e., [111] and  $[-111]$ ) are visible and VLs along the corresponding {111} planes are observed and highlighted with dashed red and purple lines. The presence of well-defined crystalline planes aligns with the schematic description, reinforcing the understanding of GST's crystallization behavior and orientation preference.

Our ordered structures closely resemble PCM superlattices [48–50] and t-GST [51, 52]. By leveraging the phase diagram shown in Figure 1a, we selected c-uni  $\text{Ge}_3\text{Sb}_2\text{Te}_6$  as the active layer for memory devices, which were fabricated using MBE. This specific composition was chosen to enable a meaningful comparison with the electrical characterization reported in Ref [53], where a polycrystalline  $\text{Ge}_3\text{Sb}_2\text{Te}_6$  was used in the memory cell.

The deposition of the chalcogenide film was carried out on a dedicated vehicle (illustrated in Figure 4a) that featured metal plugs with a contact area of  $50 \times 50 \text{ nm}^2$ . Special care was taken to have the surface of this vehicle composed solely of amorphous materials. No external interference took place in the formation of the crystalline structure during the deposition process.

Prior to deposition, the substrates underwent thorough chemical cleaning to remove any contaminants. The substrates were then loaded into the load-lock chamber of the MBE system, where they were heated to 150°C for 30 min to outgas any residual molecules or contaminants from the surface. Following this initial cleaning, the substrates were transferred to a second chamber, where a further out-gassing was performed at 350°C for an additional 30 min. This dual out-gassing process ensured that the substrates were best prepared and free of most impurities that could affect the quality of the GST film. The substrates were then finally transferred to the deposition chamber, which was maintained with a base pressure of  $2 \times 10^{-10}$  mbar. Unlike the films grown on Sb passivated reconstructed Si, the surface of the test vehicle does not present a surface that would allow the ordered growth of GST. Therefore, to obtain a textured film, we employed a well-known “two-step approach” [37, 54, 55]: before GST deposition, a 5 nm  $\text{Sb}_2\text{Te}_3$  buffer layer was deposited at 50°C, i.e., below its crystallization temperature, resulting in an amorphous film. During subsequent heating to 250°C, the substrate was exposed to a Te flux to prevent  $\text{Sb}_2\text{Te}_3$  desorption. The  $\text{Sb}_2\text{Te}_3$  layer crystallized at around 70°C, thereby providing a suitable template for the textured growth of GST at 250°C.

For the structural characterization of the deposited films, in situ Reflection High-Energy Electron Diffraction (RHEED) was employed. The RHEED pattern, captured after the deposition of the GST layer, is shown in Figure 4a. The pattern revealed sharp and distinct diffraction streaks, which are the hallmark of a high degree of in-plane ordering and crystallographic texture in the GST films. The presence of small, superimposed spots in

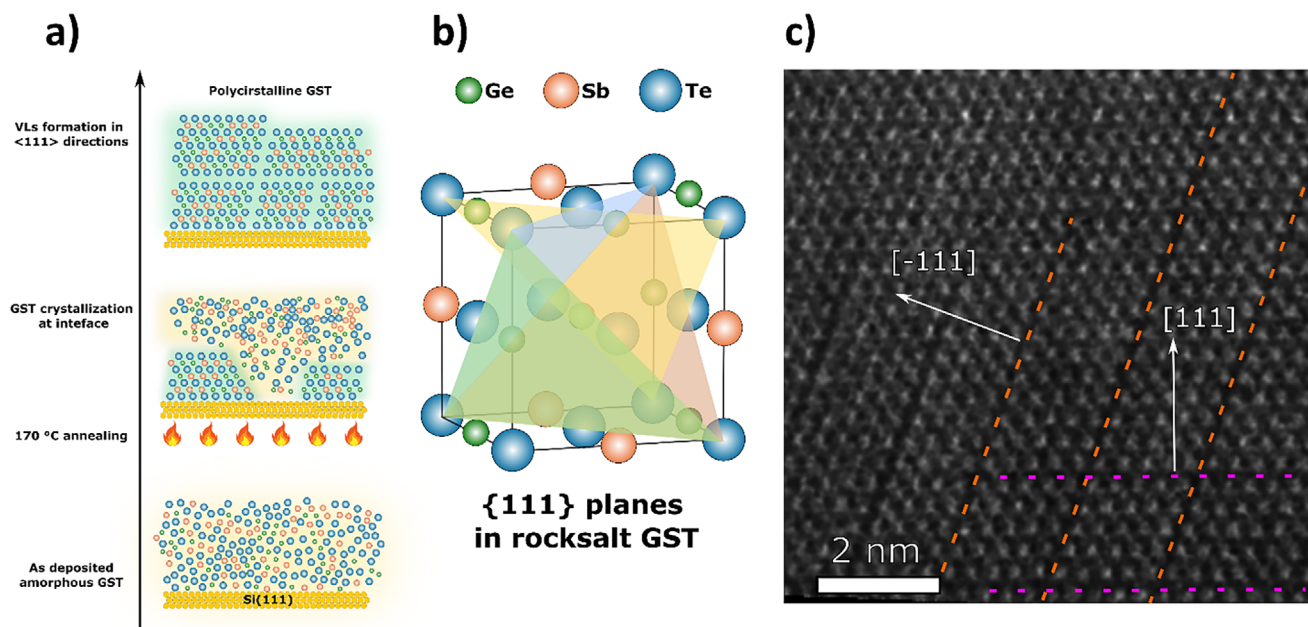


**FIGURE 3** | (a) Schematic of polycrystalline growth of GST, obtained by depositing and annealing an amorphous sample on Sb-passivated Si(111), showing structural evolution upon annealing at 170 °C, leading to polycrystalline GST with vacancies ordered in layers (VLS) or vertical lamellae aligned in the [111] directions. (b) ball-and-stick model of the rocksalt GST lattice with Ge (green), Sb (orange), and Te (blue) atoms, highlighting the 4 possible {111} planes in which vacancies can accumulate to form VLS. (c) HAADF STEM micrograph of the polycrystalline GST sample, grown as specified in (a) and oriented along the cubic [1–10] Z.A. In this orientation, two [111] directions are visible and VLS along the corresponding {111} planes are observed (overlaid orange and purple dashed lines).

the pattern indicates localized scattering from nano-scale surface protrusions, which is consistent with a textured crystalline film that also exhibits a limited degree of nanoscale roughness. The stability of the RHEED pattern further underscores that the ordering is not transient but intrinsic to the film. Taken together, these observations confirm that our growth diagram is effective in guiding the reproducible growth of ordered GST films, even on amorphous substrates where achieving such texturing is non-trivial.

The electrical characterization of the memory devices was conducted through current–voltage ( $I$ – $V$ ) measurements for both textured and polycrystalline GST-based cells, as shown in Figure 4b. For a device initially in the high resistive state (amorphous GST), voltage pulses were applied while measuring the induced current. The magnitude of the applied voltage was increased stepwise, as shown in Figure 4b, providing the characteristic  $I$ – $V$  curve associated to the crystallization of GST, leading the cell into the low resistive state. The curve displays the expected threshold voltage switching behavior, with a voltage slightly above 1 V, which was marginally higher than the switching voltage observed in polycrystalline GST.

To further investigate the performance of MBE-grown GST, Resistance-Current (R–I) measurements were conducted during the transition from the low resistive state (filled symbols) to the high resistive state (empty symbols) [Figure 4c]. Both curves showed a change in resistivity by several orders of magnitude as a consequence of the programming procedure. In comparison to devices based on untextured polycrystalline GST, the power consumption during the transition was lower for devices fabricated with textured GST, highlighting the better performance

for the latter. The lower  $I_{\text{reset}}$  observed in highly-textured GST is likely attributed to the presence of VL/vdW gaps, which enhance thermal confinement within the active material [50, 56].

### 3 | Conclusions

The growth of GST alloys is a complex process governed by the interplay of composition, phase, and ordering. By systematically varying  $\Phi_{\text{Te}}$  and  $T_{\text{sub}}$ , we have mapped out a growth diagram that highlights the conditions required to achieve specific GST compositions and phases. Our findings demonstrate that increasing  $\Phi_{\text{Te}}$  or decreasing  $T_{\text{sub}}$  enhances ordering, favoring the transition from c- to t- GST. The stabilization of specific phases depends on Te incorporation in the films, with GST225 emerging as the most favorable composition, followed by GST124 and GST326. Local structural analysis using STEM-HAADF confirms that different GST phases exhibit distinct atomic arrangements and Te-Te plane distances, reinforcing the role of vdW gaps in determining structural stability. Furthermore, the observation of ordered c-phases during annealing suggests a possible transition pathway from amorphous GST. These insights provide a deeper understanding of the growth mechanisms governing GST alloys and serve as a valuable guide for tailoring material properties for phase-change memory and other applications.

Our investigation into the impact of composition and structure on the transport properties of GST alloys reveals key distinctions between c- and t-phase samples. Some GST alloys have been predicted to be TIs, and so a surface conducting state is expected to be present, plausibly affecting the resistance of the phase change states when the size of the memory cells is reduced to

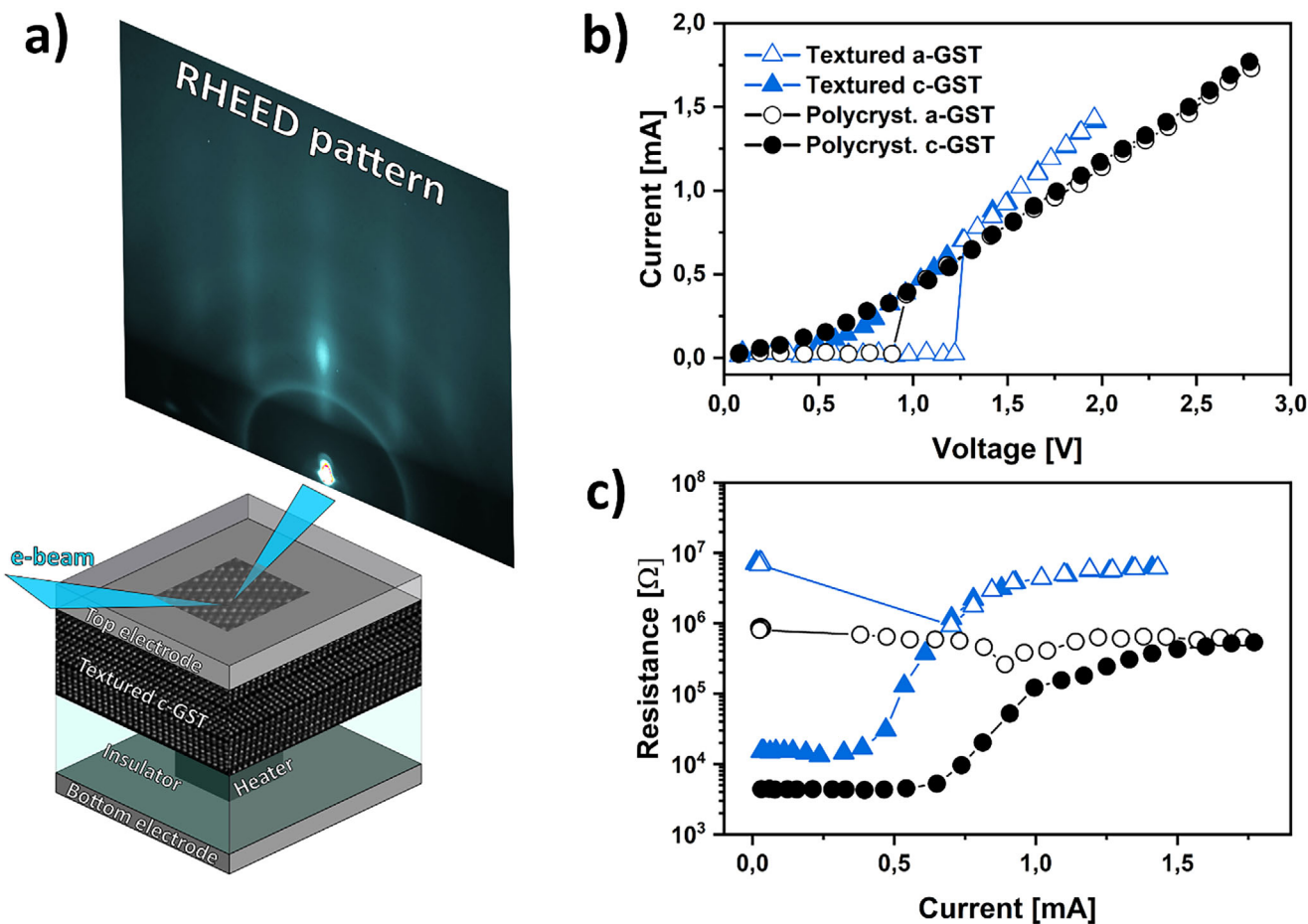


**FIGURE 4** | (a) Schematic of the experimental setup depicting the RHEED electron beam interacting with the GST layer within a device stack composed of electrodes, an insulator, and a heater. RHEED pattern taken after the deposition of the ordered crystalline GST (c-GST) layer. Please note that the top electrode was deposited after RHEED imaging. (b) Current-voltage of textured GST (triangles) and poly-untextured GST (circles) [53]. (c) Resistance as a function of increasing programming current starting from the low resistance to high resistance state of textured GST as compared to poly-untextured GST.

nanometer scales. The quantum interference effect manifested as WAL indicates that the surface state is strongly coupled with the bulk state, or the role of the surface state is insignificant in comparison to that of the bulk state, due to the metallic conduction of the GST alloys. However, the marked differences in mobility and sheet resistance between c- and t-GST underscore the influence of vacancy ordering and structural anisotropy on transport mechanisms. The observed resistivity drop between c- and t-samples is attributed to the transformation of degenerate VLs into vdW layers, leading to a shift from isotropic to anisotropic conduction. This reconfiguration reduces bulk-surface scattering in t-GST, resulting in enhanced mobility. The findings emphasize the role of vacancy ordering in tuning transport properties and suggest that band structure modifications, including possible topological effects, warrant further theoretical investigation.

Through electrical characterization, we show that textured MBE-grown GST films exhibit stable and reversible switching between amorphous and crystalline states. Importantly, resistance-current (R-I) measurements reveal a reduction in  $I_{\text{reset}}$  during the phase transition. These results provide evidence that MBE-grown ordered GST could improve device energy efficiency.

## 4 | Methods

### 4.1 | Thin Film Growth

The GST reported in the phase diagram, as well as those for magneto transport measurements, were grown by MBE on Sb-passivated Si(111)-(7 × 7) surface (i.e., Si(111)-(Si(111)-(√3 × √3)R30°-Sb). Details on the substrate preparation for obtaining such passivation can be found elsewhere [34]. All sample growths are performed under comparable Ge and Sb fluxes ( $\Phi_{\text{Ge}} = 0.055$  nm/min,  $\Phi_{\text{Sb}} = 0.193$  nm/min) and increasing Te flux and/or growth temperature. These fluxes, as well as those in our growth diagram, are reported in terms of effective deposition rate, as measured at the growth position, to quantify and compare fluxes across different MBE systems. The base pressure of the growth chamber was as low as  $2 \times 10^{-10}$  mbar. Further details on growth, XRD, and Raman characterization can be found at ref [16]. As for the notation of crystallographic planes, directions, and zone axes: for the cubic phase, we use the standard cubic notation, whereas for the trigonal phase, we adopt the hexagonal indexation.

Concerning the growth of GST films for device characterization, the deposition was carried out on a dedicated vehicle characterized by metal plugs with a contact area of  $50 \times 50 \text{ nm}^2$ . Prior to deposition, the chip was heated to  $150^\circ\text{C}$  for 30 min to outgas any residual molecules or contaminants from the surface and then transferred to a second chamber, where a further outgassing was performed at  $350^\circ\text{C}$  for 30 more minutes. Finally, the substrates were transferred to the deposition chamber. Here, an amorphous 5 nm  $\text{Sb}_2\text{Te}_3$  buffer layer was first deposited at  $50^\circ\text{C}$ . Subsequently, the substrate was heated to  $250^\circ\text{C}$  (heating rate =  $0.3^\circ\text{C}/\text{min}$ ), under Te flux to prevent  $\text{Sb}_2\text{Te}_3$  desorption, triggering the crystallization of such a layer, thus providing a suitable template for the textured growth of GST [57]. The deposition of GST occurred at  $250^\circ\text{C}$ .

## 4.2 | Magneto Transport Measurements

The van-der-Pauw method was used for the transport characterization of the films in obtaining the electrical resistivity and the hole concentration. Patterning the films to Hall bars was intentionally avoided to prevent surface contamination in the processing. The nearly square-shaped pieces of the samples had a size of several millimeters. The ohmic contacts were prepared at the four corners of the sample pieces by the deposition of an Au layer. The magneto transport measurements were carried out at a temperature of 4K using an “attocube systems AG” combined with a liquid helium-based bath cryostat with a superconducting magnet “attoLIQUID 1000”. For the WAL effect, the longitudinal conductivity was calculated at zero magnetic field. The conductivity in the presence of the magnetic field was estimated by measuring one four-terminal resistance in the van-der-Pauw configuration, assuming that the ratio between the two van-der-Pauw resistances did not change with the magnetic field.

## 4.3 | Scanning Transmission Electron Microscopy

Local sample structure was investigated by scanning transmission electron microscopy (STEM). The analyses were performed by using a JEOL ARM200F Cs-corrected microscope, equipped with a cold-field emission gun and operating at 200 keV. Micrographs were acquired in Z-contrast mode by high-angle annular dark field (HAADF).

## 4.4 | Memory Devices Electrical Characterization

Electrical characterization was carried out using an Agilent 81110 pulse generator to apply fast programming pulses to the cell, while a Le Croy 9350A oscilloscope recorded the voltage drop across the device. The programmed-state readout in the DC regime was performed with a Keithley 236 parameter analyzer through an automatically switched AC/DC circuit. More details on electrical characterization can be found in ref [49, 53].

### Author Contributions

The paper was written by V.B., R.M., and R.C., with help and contributions from all co-authors. V.B. and F.A. performed the growth and XRD charac-

terization of the samples. V.B. F.A., and R.C. performed the interpretation of growth experiments. V.B. and Y.T. performed the magneto-transport measurements. A.M.M. performed the HAADF STEM characterization. S.P. contributed to data interpretation, prepared all figures, and prepared the final draft. All authors have given approval to the final version of the manuscript. The project was initiated and conceptualized by R.C.

### Acknowledgements

We gratefully acknowledge A. Redaelli and M. Boniardi for the insightful discussions. We thank C. Stemmler for technical support at the MBE system and D. Czubak for the support with the magneto transport setup. This work was partially supported by the national project, BEYOND NANO Upgrade (CUP G66J17000350007) and by NextGenerationEU, M4C2, within the PNRR project NFFA—DI, CUP B53C22004310006, IR0000015, having benefited from the access provided by CNR—IMM@CT in Catania. European Union’s project PASTRY (GA 317746), Horizon 2020 Research and Innovation program, Grant Agreement No. 824957—Project Before-Hand. Italian Ministry of University and Research (MUR) through project PRIN2020—Emphasis—20203K2T7F\_004.

### Conflicts of Interest

The authors declare no conflict of interest.

### Data Availability Statement

The data that support the findings of this study are available from the corresponding author upon reasonable request.

### References

1. A. Soumyanarayanan, N. Reyren, A. Fert, and C. Panagopoulos, “Emergent Phenomena Induced by Spin–Orbit Coupling at Surfaces and Interfaces,” *Nature* 539 (2016): 509–517, <https://doi.org/10.1038/nature19820>.
2. P. Cheng, C. Song, T. Zhang, et al., “Landau Quantization of Topological Surface States in  $\text{Bi}_2\text{Se}_3$ ,” *Physical Review Letters* 105 (2010): 076801, <https://doi.org/10.1103/PhysRevLett.105.076801>.
3. H. Lin, L. A. Wray, Y. Xia, et al., “Half-Heusler Ternary Compounds as New Multifunctional Experimental Platforms for Topological Quantum Phenomena,” *Nature Materials* 9 (2010): 546–549, <https://doi.org/10.1038/nmat2771>.
4. D. Kong, J. C. Randel, H. Peng, et al., “Topological Insulator Nanowires and Nanoribbons,” *Nano Letters* 10 (2010): 329–333, <https://doi.org/10.1021/nl903663a>.
5. Y. Takagaki, U. Jahn, A. Giussani, and R. Calarco, “Multiple State Transport Deduced by Weak Antilocalization and Electron–Electron Interaction Effects in  $\text{Sb}_x\text{Te}_{1-x}$  Layers,” *Journal of Physics: Condensed Matter* 26 (2014): 095802, <https://doi.org/10.1088/0953-8984/26/9/095802>.
6. Y. Takagaki, A. Giussani, J. Tominaga, U. Jahn, and R. Calarco, “Transport Properties in a  $\text{Sb}$ – $\text{Te}$  Binary Topological-Insulator System,” *Journal of Physics: Condensed Matter* 25 (2013): 345801, <https://doi.org/10.1088/0953-8984/25/34/345801>.
7. H. Zhang, C. Liu, X. Qi, X. Dai, Z. Fang, and S. Zhang, “Topological Insulators in  $\text{Bi}_2\text{Se}_3$ ,  $\text{Bi}_2\text{Te}_3$  and  $\text{Sb}_2\text{Te}_3$  With a Single Dirac Cone on the Surface,” *Nature Physics* 5 (2009): 438–442, <https://doi.org/10.1038/nphys1270>.
8. J. Tominaga, A. V. Kolobov, P. Fons, T. Nakano, and S. Murakami, “Ferroelectric Order Control of the Dirac-Semimetal Phase in  $\text{GeTe}$ – $\text{Sb}_2\text{Te}_3$  Superlattices,” *Advanced Materials Interfaces* 1 (2014): 1300027, <https://doi.org/10.1002/admi.201300027>.
9. B. Sa, J. Zhou, Z. Sun, J. Tominaga, and R. Ahuja, “Topological Insulating in  $\text{GeTe}/\text{Sb}_2\text{Te}_3$  Phase-Change Superlattice,” *Physical Review Letters* 109 (2012): 096802, <https://doi.org/10.1103/PhysRevLett.109.096802>.

10. L. Gallo, et al., "A 64-core Mixed-signal in-memory Compute Chip Based on Phase-change Memory for Deep Neural Network Inference," *Nature Electronics* 6 (2023): 680–693, <https://doi.org/10.1038/s41928-023-01010-1>.
11. V. Joshi, M. Le Gallo, S. Haefeli, et al., "Accurate Deep Neural Network Inference Using Computational Phase-change Memory," *Nature Communications* 11 (2020): 2473, <https://doi.org/10.1038/s41467-020-16108-9>.
12. T. Matsunaga, N. Yamada, and Y. Kubota, "Structures of stable and metastable Ge<sub>2</sub>Sb<sub>2</sub>Te<sub>5</sub>, an intermetallic compound in GeTe–Sb<sub>2</sub>Te<sub>3</sub> pseudobinary systems," *Acta Crystallographica Section B Structural Science* 60 (2004): 685–691, <https://doi.org/10.1107/S0108768104022906>.
13. W. Zhang, H. Zhang, S. Sun, et al., "Metavalent Bonding in Layered Phase-Change Memory Materials," *Advanced Science* 10 (2023): 2300901, <https://doi.org/10.1002/advs.202300901>.
14. W. Zhang, A. Thiess, P. Zalden, et al., "Role of Vacancies in Metal–Insulator Transitions of Crystalline Phase-Change Materials," *Nature Materials* 11 (2012): 952–956, <https://doi.org/10.1038/nmat3456>.
15. T. Jiang, X. Wang, J. Wang, et al., "In Situ Characterization of Vacancy Ordering in Ge–Sb–Te Phase-change Memory Alloys," *Fundamental Research* 4 (2024): 1235–1242, <https://doi.org/10.1016/j.fmre.2022.09.010>.
16. V. Bragaglia, F. Arciprete, A. M. Mio, and R. Calarco, "Designing Epitaxial GeSbTe Alloys by Tuning the Phase, the Composition, and the Vacancy Ordering," *Journal of Applied Physics* 123 (2018): 215304, <https://doi.org/10.1063/1.5024047>.
17. A. Lotnyk, T. Dankwort, M. Behrens, L. Voß, S. Cremer, and L. Kienle, "In Situ Atomic-scale Observation of Transformation From Disordered to Ordered Layered Structures in Ge–Sb–Te Phase Change Memory Thin Films," *Acta Materialia* 266 (2024): 119670, <https://doi.org/10.1016/j.actamat.2024.119670>.
18. V. Bragaglia, F. Arciprete, W. Zhang, et al., "Metal-insulator Transition Driven by Vacancy Ordering in GeSbTe Phase Change Materials," *Scientific Reports* 6 (2016): 23843, <https://doi.org/10.1038/srep23843>.
19. V. Bragaglia, K. Hollmack, J. E. Boschker, et al., "Far-infrared and Raman Spectroscopy Investigation of Phonon Modes in Amorphous and Crystalline Epitaxial GeTe–Sb<sub>2</sub>Te<sub>3</sub> Alloys," *Scientific Reports* 6 (2016): 28560, <https://doi.org/10.1038/srep28560>.
20. J. Kim, J. Kim, and S. Jhi, "Prediction of Topological Insulating Behavior in Crystalline Ge–Sb–Te," *Physical Review B* 82 (2010): 201312, <https://doi.org/10.1103/PhysRevB.82.201312>.
21. J. Kim, J. Kim, K. Kim, and S. Jhi, "Topological Phase Transition in the Interaction of Surface Dirac Fermions in Heterostructures," *Physical Review Letters* 109 (2012): 146601, <https://doi.org/10.1103/PhysRevLett.109.146601>.
22. I. I. Petrov, R. M. Imamov, and Z. G. Pinsker, "Electron-diffraction Determination of the Structures of Ge<sub>2</sub>Sb<sub>2</sub>Te<sub>5</sub> and GeSb<sub>4</sub>Te<sub>7</sub>," *Soviet Physics Crystallography* 13 (1968): 339–342.
23. B. Kooi and J. T. M. De Hosson, "Electron Diffraction and High-Resolution Transmission Electron Microscopy of the High Temperature Crystal Structures of GexSb<sub>2</sub>Te<sub>3+x</sub> (x=1,2,3) Phase Change Material," *Journal of Applied Physics* 92 (2002): 3584–3590, <https://doi.org/10.1063/1.1502915>.
24. B. Sa, J. Zhou, Z. Song, Z. Sun, and R. Ahuja, "Pressure-induced Topological Insulating Behavior in the Ternary Chalcogenide Ge<sub>2</sub>Sb<sub>2</sub>Te<sub>5</sub>," *Physical Review B* 84 (2011): 085130, <https://doi.org/10.1103/PhysRevB.84.085130>.
25. B. Sa, J. Zhou, Z. Sun, and R. Ahuja, "Strain-induced Topological Insulating Behavior in Ternary Chalcogenide Ge<sub>2</sub>Sb<sub>2</sub>Te<sub>5</sub>," *EPL (Europhysics Letters)* 97 (2012): 27003, <https://doi.org/10.1209/0295-5075/97/27003>.
26. I. V. Silkin, Y. M. Koroteev, G. Bihlmayer, and E. V. Chulkov, "Influence of the Ge–Sb Sublattice Atomic Composition on the Topological Electronic Properties of Ge<sub>2</sub>Sb<sub>2</sub>Te<sub>5</sub>," *Applied Surface Science* 267 (2013): 169–172, <https://doi.org/10.1016/j.apsusc.2012.09.017>.
27. J. Kim and S. Jhi, "Disorder-induced Structural Transitions in Topological Insulating Ge–Sb–Te Compounds," *Journal of Applied Physics* 117 (2015): 195701, <https://doi.org/10.1063/1.4921294>.
28. T. Siegrist, P. Jost, H. Volker, et al., "Disorder-induced Localization in Crystalline Phase-change Materials," *Nature Materials* 10 (2011): 202–208, <https://doi.org/10.1038/nmat2934>.
29. H. Volker, P. Jost, and M. Wuttig, "Low-Temperature Transport in Crystalline Ge<sub>1</sub>Sb<sub>2</sub>Te<sub>4</sub>," *Advanced Functional Materials* 25 (2015): 6390–6398, <https://doi.org/10.1002/adfm.201500830>.
30. E. Jos, "Boschker & Raffaella Calarco. Growth of Crystalline Phase Change Materials by Physical Deposition Methods," *Adv in Phys X* 2 (2017): 675–694.
31. M. Liebmann, C. Rinaldi, D. Di Sante, et al., "Giant Rashba-Type Spin Splitting in Ferroelectric GeTe(111)," *Advanced Materials* 28 (2016): 560.
32. J. Krempaský, H. Volfová, S. Muff, et al., "Disentangling Bulk and Surface Rashba Effects in Ferroelectric  $\alpha$ -GeTe," *Physical Review B* 94 (2016): 205111, <https://doi.org/10.1103/PhysRevB.94.205111>.
33. C. Pauly, M. Liebmann, A. Giussani, et al., "Evidence for Topological Band Inversion of the Phase Change Material Ge<sub>2</sub>Sb<sub>2</sub>Te<sub>5</sub>," *Applied Physics Letters* 103 (2013): 243109, <https://doi.org/10.1063/1.4847715>.
34. J. E. Boschker, J. Momand, V. Bragaglia, et al., "Surface Reconstruction-Induced Coincidence Lattice Formation between Two-Dimensionally Bonded Materials and a Three-Dimensionally Bonded Substrate," *Nano Letters* 14 (2014): 3534–3538, <https://doi.org/10.1021/nl5011492>.
35. R. Wang, J. E. Boschker, E. Bruyer, et al., "Toward Truly Single Crystalline GeTe Films: The Relevance of the Substrate Surface," *The Journal of Physical Chemistry C* 118 (2014): 29724–29730, <https://doi.org/10.1021/jp507183f>.
36. R. Wang, V. Bragaglia, J. E. Boschker, and R. Calarco, "Intermixing During Epitaxial Growth of van der Waals Bonded Nominal GeTe/Sb<sub>2</sub>Te<sub>3</sub> Superlattices," *Crystal Growth & Design* 16 (2016): 3596–3601, <https://doi.org/10.1021/acs.cgd.5b01714>.
37. S. Prili, V. Bragaglia, V. P. Jonnalagadda, et al., "Understanding the Growth and Properties of Sputter-Deposited Phase-Change Superlattice Films," *Advanced Materials Interfaces* 12 (2025): 2500058, <https://doi.org/10.1002/admi.202500058>.
38. M. Behrens, A. Lotnyk, U. Roß, et al., "Impact of Disorder on Optical Reflectivity Contrast of Epitaxial Ge<sub>2</sub>Sb<sub>2</sub>Te<sub>5</sub> Thin Films," *CrystEngComm* 20 (2018): 3688–3695, <https://doi.org/10.1039/C8CE00534F>.
39. L. E. Shelimova, O. G. Karpinskii, M. A. Kretova, et al., "Homologous Series of Layered Tetradymite-Like Compounds in the Sb–Te and GeTe–Sb<sub>2</sub>Te<sub>3</sub> Systems," *Inorganic Materials* 36 (2000): 768–775, <https://doi.org/10.1007/BF02758595>.
40. G. Bergmann, "Weak Localization in Thin Films," *Physics Reports* 107 (1984): 1–58, [https://doi.org/10.1016/0370-1573\(84\)90103-0](https://doi.org/10.1016/0370-1573(84)90103-0).
41. S. Hikami, A. I. Larkin, and Y. Nagaoka, "Spin-Orbit Interaction and Magnetoresistance in the Two Dimensional Random System," *Progress of Theoretical Physics* 63 (1980): 707–710.
42. Y. Takagaki, "Conductance Fluctuations Induced by Bulk state in Quasi-one-dimensional Strips of Topological Insulator," *Physical Review B* 85 (2012): 155308, <https://doi.org/10.1103/PhysRevB.85.155308>.
43. H. He, G. Wang, T. Zhang, et al., "Impurity Effect on Weak Antilocalization in the Topological Insulator Bi<sub>2</sub>Te<sub>3</sub>," *Physical Review Letters* 106 (2011): 166805, <https://doi.org/10.1103/PhysRevLett.106.166805>.
44. A. M. Mio, S. M. S. Privitera, V. Bragaglia, et al., "Role of Interfaces on the Stability and Electrical Properties of Ge<sub>2</sub>Sb<sub>2</sub>Te<sub>5</sub> Crystalline Structures," *Scientific Reports* 7 (2017): 2616, <https://doi.org/10.1038/s41598-017-02710-3>.
45. P. P. Konstantinov, L. E. Shelimova, E. S. Avilov, M. A. Kretova, and V. S. Zemskov, "Thermoelectric Properties of nGeTe mSb<sub>2</sub>Te<sub>3</sub>Layered

- Compounds,” *Inorganic Materials* 37 (2001): 662–668, <https://doi.org/10.1023/A:1017613804472>.
46. L. E. Shelimova, O. G. Karpinskii, P. P. Konstantinov, M. A. Kretova, E. S. Avilov, and V. S. Zemskov, “Composition and Properties of Layered Compounds in the GeTe–Sb<sub>2</sub>Te<sub>3</sub> System,” *Inorganic Materials* 37 (2001): 342–348, <https://doi.org/10.1023/A:1017519625907>.
47. Y. Takagaki, A. Giussani, K. Perumal, R. Calarco, and K. Friedland, “Robust Topological Surface States in Sb<sub>2</sub>Te<sub>3</sub> Layers as Seen From the Weak Antilocalization Effect,” *Physical Review B* 86 (2012): 125137, <https://doi.org/10.1103/PhysRevB.86.125137>.
48. R. E. Simpson, P. Fons, A. V. Kolobov, et al., “Interfacial Phase-change Memory,” *Nature Nanotechnology* 6 (2011): 501–505, <https://doi.org/10.1038/nnano.2011.96>.
49. M. Boniardi, et al., “Evidence for Thermal-Based Transition in Super-Lattice Phase Change Memory,” *physica status solidi–Rapid Research Letters* 13 (2019): 1800634.
50. H. Kwon, A. I. Khan, C. Perez, M. Asheghi, E. Pop, and K. E. Goodson, “Uncovering Thermal and Electrical Properties of Sb<sub>2</sub>Te<sub>3</sub>/GeTe Superlattice Films,” *Nano Letters* 21 (2021): 5984–5990, <https://doi.org/10.1021/acs.nanolett.1c00947>.
51. G. Cohen, et al., “Low Reset Current Mushroom Cell Phase-change Memory (PCM) Using fiber-textured Homostructure GeSbTe on Highly Oriented Seed Layer,” *physica status solidi–Rapid Research Letters* 8 (2024): 2300426.
52. D. Térébéneç, F. Hippert, N. Bernier, N. Castellani, and P. Noé, “GeTe/Sb<sub>2</sub>Te<sub>3</sub> Super-Lattices: Impact of Atomic Structure on the RESET Current of Phase-Change Memory Devices,” *Adv Electron Mater* 11 (2025): 2400290.
53. J. E. Boschker, M. Boniardi, A. Redaelli, H. Riechert, and R. Calarco, “Electrical Performance of Phase Change Memory Cells With Ge<sub>3</sub>Sb<sub>2</sub>Te<sub>6</sub> Deposited by Molecular Beam Epitaxy,” *Applied Physics Letters* 106 (2015): 023117, <https://doi.org/10.1063/1.4906060>.
54. Y. Saito, P. Fons, L. Bolotov, N. Miyata, A. V. Kolobov, and J. Tominaga, “A Two-step Process for Growth of Highly Oriented Sb<sub>2</sub>Te<sub>3</sub> Using Sputtering,” *AIP Advances* 6 (2016): 045220, <https://doi.org/10.1063/1.4948536>.
55. Y. Saito, M. Morota, K. Makino, J. Tominaga, A. V. Kolobov, and P. Fons, “Recent Developments Concerning the Sputter Growth of Chalcogenide-based Layered Phase-change Materials,” *Materials Science in Semiconductor Processing* 135 (2021): 106079, <https://doi.org/10.1016/j.mssp.2021.106079>.
56. A. I. Khan, X. Wu, C. Perez, et al., “Unveiling the Effect of Superlattice Interfaces and Intermixing on Phase Change Memory Performance,” *Nano Letters* 22 (2022): 6285–6291, <https://doi.org/10.1021/acs.nanolett.2c01869>.
57. J. E. Boschker, E. Tisbi, E. Placidi, et al., “Textured Sb<sub>2</sub>Te<sub>3</sub> Films and GeTe/Sb<sub>2</sub>Te<sub>3</sub> Superlattices Grown on Amorphous Substrates by Molecular Beam Epitaxy,” *AIP Advances* 7 (2017): 015106, <https://doi.org/10.1063/1.4974464>.